J. Fluid Mech. (2010), *vol.* 653, *pp.* 273–299.
doi:10.1017/S0022112010000273

Optimal linear growth in magnetohydrodynamic duct flow

DMITRY KRASNOV[1]†, OLEG ZIKANOV[2], MAURICE ROSSI[3,4] AND THOMAS BOECK[1]

[1]Institute of Thermodynamics and Fluid Mechanics, Technische Universität Ilmenau, Postfach 100565, 98684 Ilmenau, Germany

[2]Department of Mechanical Engineering, University of Michigan–Dearborn, 4901 Evergreen Road, Dearborn, MI 48128-1491, USA

[3]UPMC Univ Paris 06, UMR 7190, Institut Jean Le Rond d'Alembert, F-75005 Paris, France

[4]CNRS, UMR 7190, Institut Jean Le Rond d'Alembert, F-75005 Paris, France

(Received 8 October 2009; revised 12 January 2010; accepted 12 January 2010; first published online 16 April 2010)

Transient linear growth in laminar magnetohydrodynamic duct flow is analysed. The duct is straight with rectangular cross-section and electrically insulating walls. The applied uniform magnetic field is oriented perpendicular to the mean flow direction and parallel to one of the walls. Optimal perturbations and their maximum amplifications over finite time intervals are computed. The optimal perturbations are increasingly damped by the magnetic field, localized in the boundary layers parallel to the magnetic field irrespective of the duct aspect ratio. Typically, the optimal perturbations have non-vanishing streamwise wavenumber as found in magnetohydrodynamic channel flow with spanwise magnetic field. The Hartmann boundary layers perpendicular to the magnetic field do not contribute to the transient growth.

1. Introduction

Even though their Reynolds number (Re) is typically large, technological magnetohydrodynamic (MHD) flows are found in transitional or weakly turbulent states much more often than non-magnetic flows. This is because the imposed static magnetic field suppresses turbulence and instabilities. For instance, in continuous casting of steel slabs (see, e.g., Cukierski & Thomas 2008), intense (0.1–0.5 T) magnetic fields are imposed to suppress turbulent feeding jets and to damp turbulent eddies in the mould. For growing large silicon crystals by the Czochralsky method, magnetic fields are used to achieve better quality of the crystal through suppression of undesired fluctuations of temperature and admixture concentration and establishing a favourable temperature gradient near the solidification surface (von Ammon *et al.* 2005). Turbulence suppression might be of interest for liquid-metal (Li) cooling and breeding blankets in future nuclear fusion reactors (see, e.g., Smolentsev, Moreau & Abdou 2008).

In the current paper, the flow of an electrically conducting fluid in a rectangular duct is studied in the presence of a steady uniform magnetic field parallel to two of the perfectly insulating walls. The limit of low magnetic Reynolds number is considered

† Email address for correspondence: dmitry.krasnov@tu-ilmenau.de

because it corresponds to the typical situation for industrial and laboratory liquid-metal flows.

A rectangular duct flow in the presence of a transverse magnetic field is an archetypal case of liquid-metal MHD flows. Albeit simple, the configuration incorporates the main features of technological liquid-metal flows: magnetic suppression and anisotropy, strong mean shear and specific MHD boundary layers. As a matter of fact, the pioneering study of the duct flow by Hartmann & Lazarus (1937) is considered by many as the starting point of liquid-metal magnetohydrodynamics as a scientific discipline. At a sufficiently strong magnetic field, the MHD base velocity develops a flat core and the mean shear, and thus the potential for instability and turbulence, is limited to the boundary layers which are of two types (see, e.g., Branover 1978; Müller & Bühler 2001): the Hartmann layers appearing at the walls perpendicular to the magnetic field and the Shercliff layers at the walls parallel to the magnetic field. Reviews of earlier works and an example of recent simulations of the duct flow can be found in the books by Müller & Bühler (2001) and Branover (1978) and the paper by Kobayashi (2008), respectively.

The problem of linear stability to exponentially growing perturbations has been solved only for few cases of MHD duct flow. A combination of wall conductivities leading to the jet-like sidewall layers was analysed by Ting *et al.* (1991). However the results of this work disagreed with the experiments of Reed & Picologlou (1989). Concerning uniformly conducting or uniformly insulating walls which are characterized by monotonic flow profiles in the boundary layers, no solution of the full linear stability problem has been reported to the knowledge of the authors. The stability analysis in the limit of strong magnetic field produces critical Reynolds numbers, which are orders of magnitude higher than those observed in experiments. The most recent example of such study is the one by Potherat (2007), where linear stability of two-dimensional approximations of sidewall layers was analysed.

This discrepancy is also observed for other wall-bounded parallel shear flows. In purely hydrodynamic flows (classical pipe, duct and channel flows), turbulence appears at much lower Reynolds number than predicted by the analysis of exponentially growing perturbations. The currently accepted explanation is the concept of bypass transition based on the understanding that because of the non-normality of the linearized operator, a non-normal mode which is a combination of eigenfunctions can experience transient algebraic growth even if every eigenmode eventually decays. An essential physical mechanism of the growth is the 'lift-up effect', namely the redistribution of the mean flow velocity by the perturbations (see, e.g., Landahl 1980). If transient amplification factors are large, the non-normal perturbation can grow to the point at which it reaches the nonlinear regime and becomes capable of modifying the base flow and rendering it temporarily unstable to secondary infinitesimal perturbations. A transition according to the bypass scenario has been demonstrated for the plane channel (by Reddy *et al.* 1998), pipe (by Zikanov 1996) and rectangular duct (by Biau, Soueid & Bottaro 2008) flows (see Schmid & Henningson 2001 for a review). In all these cases, the 'optimal' modes providing the strongest transient growth were found to have the form of streamwise-independent rolls evolving into streamwise streaks. Of course, the two-step scenario is rarely realized in a clear-cut way. The actual picture of transition is more complex. In particular, emphasis on global optimal modes in the form of streamwise rolls can be misleading. Nonlinear interaction between the suboptimal non-streamwise modes can lead to transition at lower Reynolds number and perturbation amplitude as discussed by Schmid & Henningson (2001). Nevertheless, understanding the transient growth, nonlinear modulation and breakdown is undoubtedly the key to understanding the

transition. These phenomena were also shown, for example, by Waleffe (1997) and Hof *et al.* (2005) to play a decisive role in sustaining turbulence at low and moderate Re by forming the minimal loop of rolls, streaks and travelling waves transforming into each other.

More relevant for the present paper are the results obtained for the channel flows with wall-normal (Hartmann flow) and spanwise magnetic fields. For the Hartmann flow, the optimal modes were analysed by Gerard-Varet (2002), Airiau & Castets (2004) and Krasnov *et al.* (2004). The modes were found to have the form of streamwise rolls confined to the Hartmann layers. Direct numerical simulations of the streak breakdown and subsequent transition were performed by Krasnov *et al.* (2004). It was demonstrated that weak noise added to the optimal perturbations of realistic amplitude generated transition at the values of $R = Re/Ha$, where Ha is the Hartmann number, between 350 and 400. This range of Reynolds numbers R based on the Hartmann layer thickness was in remarkable agreement with the data of the MHD duct experiments of Moresco & Alboussière (2004) as opposed to the results of the linear stability analysis of the Hartmann layer by Lingwood & Alboussière (1999) that predicted the critical value $R_c = 48\,250$.

In the case of a channel with spanwise magnetic field, the base flow retains its hydrodynamic profile, and the main effect of the magnetic field on the transition has been found (Krasnov *et al.* 2008) to be the suppression of streamwise rolls and streaks with their strong spanwise gradients. As a result, the largest amplification is no longer provided by streamwise rolls, but by rolls oriented at an oblique angle to the flow direction. The angle grows with the Hartmann number and reaches the limit corresponding to purely spanwise rolls (Tollmien–Schlichting waves) at high Ha. As was shown by Krasnov *et al.* (2008), two symmetric oblique rolls with opposite values of the spanwise wavenumber effectively trigger the transition serving as secondary perturbations to each other.

The transition behaviour in the MHD duct flow cannot be predicted by simply extrapolating the results obtained for the channel flows with transverse and spanwise magnetic fields. Firstly, the reasons are the corner interaction between the boundary layers and the limiting effect of walls in the duct flow. Secondly, the structure of sidewall layers in a duct is essentially three-dimensional and strongly different from the structure of the Poiseuille flow considered by Krasnov *et al.* (2008). The subject of the current paper is precisely to analyse the transient growth of optimal modes in the MHD duct flow. A detailed study of the optimal modes is important as a first step towards understanding the transition in general. In particular, we will determine whether or not the transient growth first occurs within the sidewall boundary layers and analyse how the results of the channel flow studies are related to the more realistic case of a duct.

The value of understanding the nature of the transient growth extends beyond the subject of transition. The optimal modes have been shown to play a role as elements of a fully developed turbulent flow. There is also a possibility that the large-scale intermittency found in the case of a channel with spanwise magnetic field by Boeck *et al.* (2008) is realized in the duct flow. In that case, the optimal modes are likely to be the dominant elements of the flow in a certain phase of the flow development. As yet another motivation of our study, we can mention the technologically important concept of electromagnetic control (suppressing or triggering) of transition. Several mechanisms of such control were suggested, for example using an array of magnets or electric promoters in the form of strips of different electric conductivity embedded into the wall (see, e.g., Smolentsev & Dajeh 1996). Knowing the spatial characteristics of optimal modes is essential for development of such control strategies.

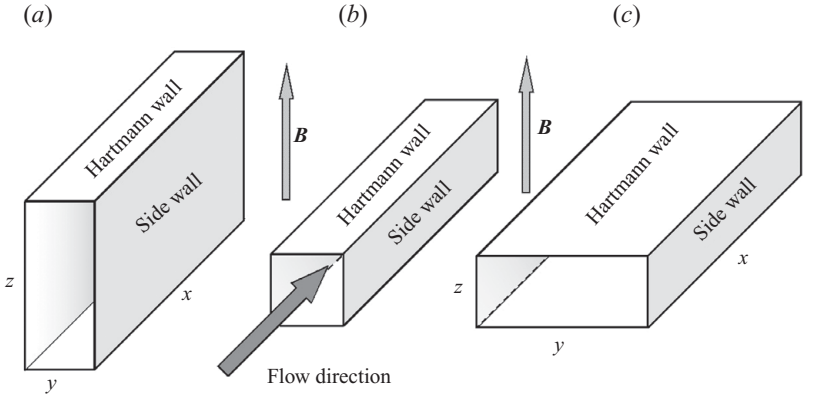

FIGURE 1. Geometry of the duct flow under magnetic field B_0: (*a*) $r \ll 1$ approaching the case of channel flow under spanwise field, (*b*) $r = 1$ square duct and (*c*) $r \gg 1$ approaching the Hartmann channel geometry.

The paper is organized as follows. After introducing the physical model and parameters in § 2, the structure of the base flow is presented in § 3. The method which determines the optimal perturbations is provided in § 4. The numerical method used to compute the optimal mode is described in § 5. Results are given in § 6. We start with the case of a square duct and continue by discussing the effect of the aspect ratio of the duct cross-section. Concluding remarks are found in § 7.

2. Physical model and parameters

We consider the flow of an electrically conducting fluid driven by an imposed constant pressure gradient in a rectangular duct. The coordinates x, y and z are in the streamwise, spanwise and cross-stream directions, respectively. The duct walls are located at $z = \pm d/2$ and $y = \pm a/2$ (see figure 1) and are assumed to be electrically insulating. The flow is subjected to a homogeneous magnetic field $\boldsymbol{B}_0 = B_0\boldsymbol{e}$, where $\boldsymbol{e} \equiv (0, 0, 1)$. The various configurations are distinguished by the aspect ratio $r = a/d$.

Other boundary conditions, for example those of perfectly conducting walls or thin walls of finite conductivity, are possible and are of interest for future analysis. Our choice of insulating walls is justified by applications in metallurgy, materials processing and blanket design for future reactors, where walls are often made of materials of low conductivity. Furthermore, considering insulating walls allows us direct comparison with the earlier studies of transient growth in channels (Gerard-Varet 2002; Airiau & Castets 2004; Krasnov *et al.* 2004, 2008).

By assuming a low magnetic Reynolds number, the governing equations can be reduced to the Navier–Stokes system for the velocity $\boldsymbol{v}$ and pressure p with an additional Lorentz force term, i.e.

$$\frac{\partial \boldsymbol{v}}{\partial t} + (\boldsymbol{v}\cdot\nabla)\boldsymbol{v} = -\frac{1}{\rho}\nabla p + \nu\nabla^2\boldsymbol{v} + \frac{1}{\rho}\boldsymbol{j}\times\boldsymbol{B}_0, \tag{2.1}$$

$$\nabla\cdot\boldsymbol{v} = 0, \tag{2.2}$$

where ν and ρ stand for kinematic viscosity and density. The induced electric current density is given by Ohm's law:

$$\boldsymbol{j} = \sigma(-\nabla\phi + \boldsymbol{v}\times\boldsymbol{B}_0), \tag{2.3}$$

where σ is the electric conductivity of the fluid. By neglecting displacement currents and assuming the fluid to be electrically neutral, it follows that the currents are solenoidal, i.e. $\boldsymbol{\nabla}\cdot\boldsymbol{j}=0$, which leads to an equation for the electric potential ϕ:

$$\nabla^2\phi = \boldsymbol{\nabla}\cdot(\boldsymbol{v}\times\boldsymbol{B}_0)\,. \tag{2.4}$$

The no-slip conditions are imposed at the walls:

$$v_x = v_y = v_z = 0 \quad \text{at } z=\pm d/2 \quad \text{and } y=\pm a/2. \tag{2.5}$$

Since no current flows through the electrically insulating walls and the velocity $\boldsymbol{v}$ is zero at these walls, (2.3) leads to

$$\frac{\partial\phi}{\partial z} = 0 \quad \text{at } z=\pm d/2, \tag{2.6}$$

$$\frac{\partial\phi}{\partial y} = 0 \quad \text{at } y=\pm a/2. \tag{2.7}$$

For non-dimensionalization, the characteristic length is taken to be half of the smaller channel width $L\equiv\min(a/2,d/2)$ and the velocity scale as the centreline velocity U_0. The scales of time and pressure are therefore taken as L/U_0 and ρU_0^2. Finally, the scales of magnetic field and electric potential are B_0 and LU_0B_0.

The non-dimensional governing equations and boundary conditions become

$$\frac{\partial\boldsymbol{v}}{\partial t} + (\boldsymbol{v}\cdot\boldsymbol{\nabla})\boldsymbol{v} = -\boldsymbol{\nabla}p + \frac{1}{Re}\nabla^2\boldsymbol{v} + N\,(-\boldsymbol{\nabla}\phi\times\boldsymbol{e} + (\boldsymbol{v}\times\boldsymbol{e})\times\boldsymbol{e})\,, \tag{2.8}$$

$$\boldsymbol{\nabla}\cdot\boldsymbol{v} = 0, \tag{2.9}$$

$$\nabla^2\phi = \boldsymbol{\nabla}\cdot(\boldsymbol{v}\times\boldsymbol{e})\,, \tag{2.10}$$

$$v_x = v_y = v_z = \frac{\partial\phi}{\partial z} = 0 \quad \text{at } z=\pm d/(2L), \tag{2.11}$$

$$v_x = v_y = v_z = \frac{\partial\phi}{\partial y} = 0 \quad \text{at } y=\pm a/(2L). \tag{2.12}$$

Three independent non-dimensional parameters appear, namely the Reynolds number

$$Re \equiv \frac{U_0 L}{\nu}, \tag{2.13}$$

the aspect ratio

$$r \equiv \frac{a}{d} \tag{2.14}$$

and the magnetic interaction parameter

$$N \equiv \frac{Ha^2}{Re}, \tag{2.15}$$

where Ha is the Hartmann number,

$$Ha \equiv LB_0\sqrt{\frac{\sigma}{\rho\nu}}. \tag{2.16}$$

The duct configurations considered in the current paper are illustrated in figure 1. In addition to the canonical case of a square duct with $r=1$, we analyse flows with $r=1/3$ and $1/9$ and flows with $r=3$ and 9. In flows with $r<1$, the magnetic field is parallel to the longer wall of the duct. The asymptotic limit at $r\to 0$ is the channel flow with spanwise magnetic field considered by Krasnov *et al.* (2008). To stress the

possible analogy, the flows in ducts with $r < 1$ are referred to as the 'spanwise case' in the remainder of the paper. In the ducts with $r > 1$, the magnetic field is directed parallel to the shorter wall. The asymptotic limit of this configuration at $r \to \infty$ is the Hartmann channel flow. Transient growth in the Hartmann channel flow was analysed by Gerard-Varet (2002), Airiau & Castets (2004) and Krasnov *et al.* (2004). Correspondingly, the term 'Hartmann case' is applied to duct flows with $r > 1$.

Note that two simulations with identical Re and Ha and aspect ratios r and $1/r$ correspond to flows in the same duct geometry with a magnetic field of equal strength but perpendicular orientations. The analysis is conducted for a single Reynolds number $Re = 5000$ and Hartmann numbers between 0 and 50.

3. Base duct flow

For the linear stability analysis we linearize the equations around a laminar base flow which is steady, purely streamwise and independent of the streamwise coordinate. It is fully described by the streamwise velocity component $U_B(y, z)$ and the electric potential $\phi_B(y, z)$, which satisfy the dimensionless equations

$$\frac{\partial^2 U_B}{\partial y^2} + \frac{\partial^2 U_B}{\partial z^2} = Ha^2 \left(\frac{\partial \phi_B}{\partial y} + U_B \right) - \lambda, \tag{3.1}$$

$$\frac{\partial^2 \phi_B}{\partial y^2} + \frac{\partial^2 \phi_B}{\partial z^2} = -\frac{\partial U_B}{\partial y}, \tag{3.2}$$

with the boundary condition

$$U_B = 0, \quad \frac{\partial \phi_B}{\partial z} = 0 \quad \text{at } z = \pm d/(2L), \tag{3.3}$$

$$U_B = 0, \quad \frac{\partial \phi_B}{\partial y} = 0 \quad \text{at } y = \pm a/(2L). \tag{3.4}$$

The value of the non-dimensional pressure gradient λ,

$$\lambda \equiv -\frac{L^2}{U_0 \nu \rho} \frac{\partial P_B}{\partial x}, \tag{3.5}$$

is not explicitly known but is implicitly given by the constraint that $U_B(0, 0) = 1$. We can bypass this problem by solving the above linear system specifying $\lambda = 1$, and the solutions for U_B and ϕ_B thus obtained are then renormalized so that $U_B(0, 0) = 1$.

The base flow is computed using the finite-difference method described in § 5. This numerical solution has been verified for all aspect ratios r and Hartmann numbers Ha considered in the present work, through a comparison with the infinite-series solution that can be found, e.g., in Müller & Bühler (2001). The structure of this flow can be found in the books of Branover (1978) and Müller & Bühler (2001). However, we provide a brief discussion of some features that have significant implications for instability and transient growth. As seen in figure 2, a sufficiently strong magnetic field leads to a base flow consisting of a flat core and MHD boundary layers. The flat core becomes more pronounced and the boundary layers become thinner with growing Hartmann number. In the spanwise case $r < 1$, the Hartmann number is defined using the spanwise half-width $a/2$, and the Hartmann layer thickness scales as $\delta_{Ha} \approx a/Ha$ and the Shercliff layer thickness as $\delta_{Sh} \approx a/r^{1/2} Ha^{1/2}$. In the Hartmann case $r > 1$, the Hartmann number is based on the width $d/2$, and we have $\delta_{Ha} \approx d/Ha$ and $\delta_{Sh} \approx d/Ha^{1/2}$.

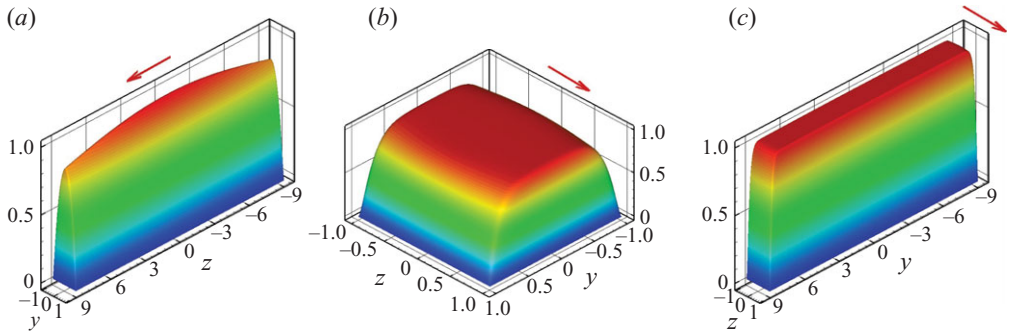

FIGURE 2. Base flow for $Ha = 50$ and $Re = 5000$: (*a*) $r = 1/9$ (spanwise case), (*b*) $r = 1$ and (*c*) $r = 9$ (Hartmann case). The arrow indicates the orientation of the applied magnetic field.

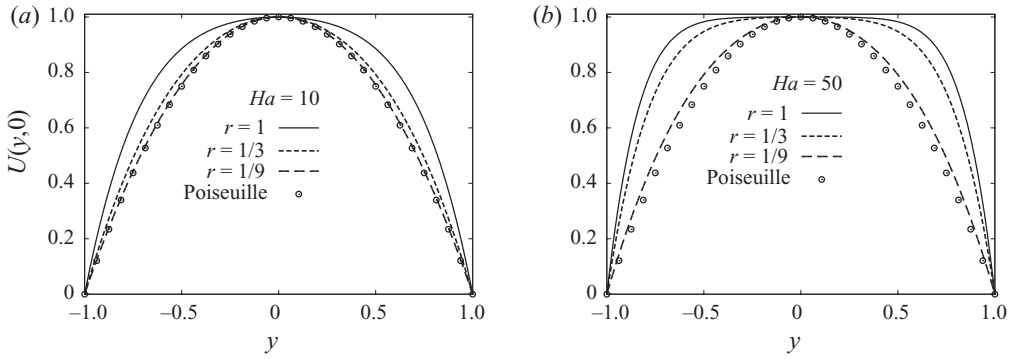

FIGURE 3. Spanwise case $r \leqslant 1$: Basic velocity profiles $U_B(y, z = 0)$ in the central cross-section parallel to the shorter walls of the duct. Plots show the cases $r = 1/9$, $r = 1/3$ and $r = 1$ with (*a*) $Ha = 10$ and (*b*) $Ha = 50$. The Poiseuille velocity profile is shown by circles to illustrate the convergence of the duct flow profiles for $r \to 0$.

The relation between the shape of the duct base flow and the two asymptotic limits of channel flow with spanwise magnetic field and channel flow with normal magnetic field is illustrated in figures 3 and 4. Base velocity profiles are shown in the central cross-section parallel to the shorter walls or, equivalently, perpendicular to the walls that become the channel walls in the asymptotic limit. Qualitatively similar behaviour is observed for non-central cross-sections, provided they are taken outside the corner areas.

It is seen in figure 3(*a*, *b*) that as r decreases, the Shercliff layers become thicker; the flat core disappears in the y direction; and the velocity profile $U(y, 0)$ approaches the parabolic Poiseuille flow profile characteristic of the channel flow with a spanwise magnetic field. Thinner Shercliff layers at higher Ha require smaller aspect ratios to achieve convergence to the parabolic profile.

It will become apparent in § 6 that the Shercliff boundary layers are the critical areas of transient growth. This is true even in the case of the duct geometries approaching the Hartmann channel, i.e. $r \gg 1$. It is, therefore, pertinent to analyse the structure of Shercliff boundary layers at $r > 1$. The profiles of the base flow velocity in the central cross-section $z = 0$ shown in figure 4(*b*, *d*) illustrate the key feature already indicated

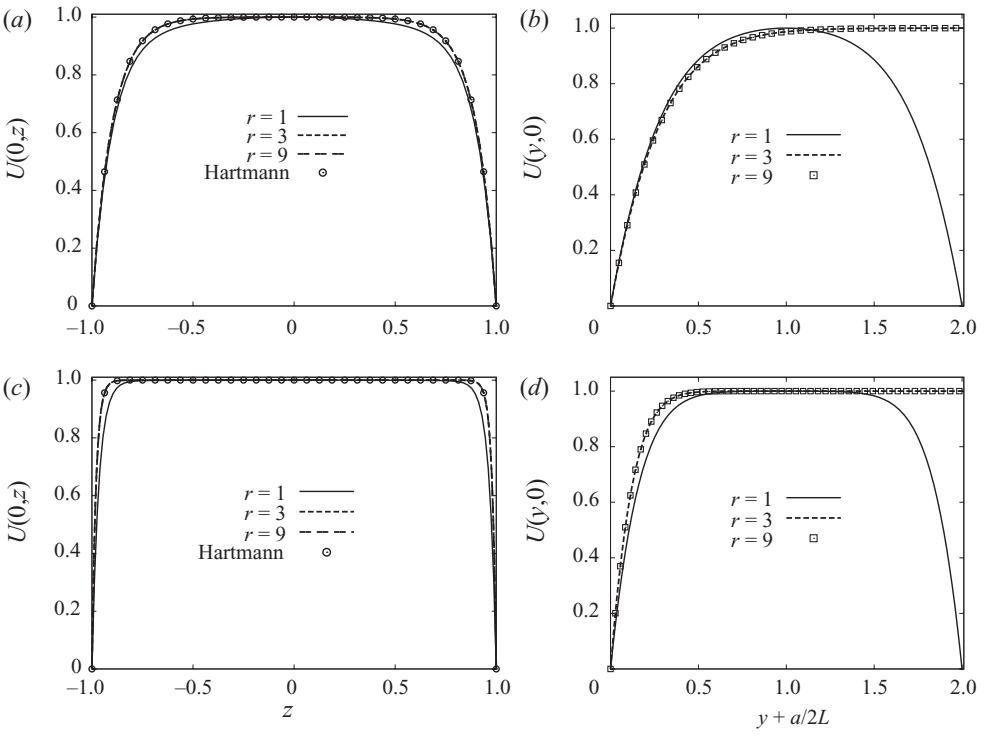

FIGURE 4. Hartmann case $r \geqslant 1$: Structure of basic velocity profiles for $Ha = 10$ (*a*,*b*) and $Ha = 50$ (*c*,*d*). Plots (*a*) and (*c*) show the basic velocity profiles $U_B(y = 0, z)$ in the central cross-section parallel to the shorter wall of the duct. The velocity profiles of Hartmann channel flow are shown by circles to illustrate the convergence of the duct flow profiles for $r \to \infty$. Plots (*b*) and (*d*) show the velocity profiles $U_B(y + a/2L, z = 0)$ within a Shercliff layer. The aspect ratio r varies from $r = 1$ to $r = 9$.

by the scaling $\delta_{Sh} \approx d/Ha^{1/2}$. The structure of the Shercliff layers changes with Ha but is practically insensitive to the size a of the duct in the direction perpendicular to the magnetic field.

4. Linear evolution of optimal perturbations

Let us now split the flow fields into the basic flow and three-dimensional perturbations as

$$\boldsymbol{v} = U_B(y, z)(1, 0, 0) + \boldsymbol{v}_p, \quad \phi = \phi_B(y, z) + \phi_p(x, y, z), \quad p = P_B(x) + p_p. \tag{4.1}$$

We linearize the system with respect to the perturbations and consider the evolution of decoupled monochromatic Fourier modes,

$$(\boldsymbol{v}_p, \phi_p, p_p) = (\hat{u}(y, z, t), \hat{v}(y, z, t), \hat{w}(y, z, t), \hat{\phi}(y, z, t), \hat{p}(y, z, t)) \exp(\mathrm{i}\alpha x), \tag{4.2}$$

where α is the streamwise wavenumber. The evolution of such infinitesimal three-dimensional perturbations is governed by the linear system

$$\left[\frac{\partial}{\partial t} + \mathrm{i}\alpha U_B\right]\hat{u} + \frac{\partial U_B}{\partial z}\hat{w} + \frac{\partial U_B}{\partial y}\hat{v} + \mathrm{i}\alpha\hat{p} - \frac{1}{Re}\left[\frac{\partial^2}{\partial z^2} + \frac{\partial^2}{\partial y^2} - \alpha^2\right]\hat{u} + N\hat{u} + N\frac{\partial\hat{\phi}}{\partial y} = 0, \tag{4.3}$$

$$\left[\frac{\partial}{\partial t}+\mathrm{i}\alpha U_B\right]\hat{v}+\frac{\partial\hat{p}}{\partial y}-\frac{1}{Re}\left[\frac{\partial^2}{\partial z^2}+\frac{\partial^2}{\partial y^2}-\alpha^2\right]\hat{v}+N\hat{v}-\mathrm{i}\alpha N\hat{\phi}=0, \tag{4.4}$$

$$\left[\frac{\partial}{\partial t}+\mathrm{i}\alpha U_B\right]\hat{w}+\frac{\partial\hat{p}}{\partial z}-\frac{1}{Re}\left[\frac{\partial^2}{\partial z^2}+\frac{\partial^2}{\partial y^2}-\alpha^2\right]\hat{w}=0, \tag{4.5}$$

$$\mathrm{i}\alpha\hat{u}+\frac{\partial\hat{v}}{\partial y}+\frac{\partial\hat{w}}{\partial z}=0, \tag{4.6}$$

$$\left[\frac{\partial^2}{\partial z^2}+\frac{\partial^2}{\partial y^2}-\alpha^2\right]\hat{\phi}-\mathrm{i}\alpha\hat{v}+\frac{\partial\hat{u}}{\partial y}=0 \tag{4.7}$$

with the boundary conditions

$$\hat{u}=\hat{v}=\hat{w}=0, \quad \frac{\partial\hat{\phi}}{\partial z}=0 \quad \text{at } z=\pm d/(2L), \tag{4.8}$$

$$\hat{u}=\hat{v}=\hat{w}=0, \quad \frac{\partial\hat{\phi}}{\partial y}=0 \quad \text{at } y=\pm a/(2L). \tag{4.9}$$

To quantify the amplification at time T, a norm, typically the kinetic energy of the perturbations, is defined. This norm can be orthogonally decomposed in a Fourier basis in the x direction, which implies that the individual contributions of each wavenumber α can be considered independently. We follow such a procedure and define the norm

$$E(T)\equiv\int(\hat{u}(y,z,T)\hat{u}^{+}(y,z,T)+\hat{v}(y,z,T)\hat{v}^{+}(y,z,T)+\hat{w}(y,z,T)\hat{w}^{+}(y,z,T))\,\mathrm{d}y\,\mathrm{d}z, \tag{4.10}$$

where the superscript $+$ denotes complex conjugation and spatial integration is performed over the entire duct section. The amplification gain of any given perturbation at time T is the ratio $E(T)/E(0)$. This quantity can be maximized over all possible initial shapes in (4.2) to give the maximum amplification $\hat{G}(\alpha, T, Ha, Re, r)$ at time T among the disturbances with specific wavenumbers α and non-dimensional parameters Ha, Re and r.

Using a Lagrangian formalism, the maximum of $E(T)/E(0)$ is determined via an optimization with two constraints: (i) the disturbance energy $E(0)$ at time $t=0$ is equal to unity; (ii) the disturbance satisfies the linear governing equations as well as the boundary conditions during the complete time interval $[0, T]$. Lagrangian multipliers – called adjoint fields – are introduced to enforce these constraints. These adjoint fields $(\tilde{u}(y,z,t), \tilde{v}(y,z,t), \tilde{w}(y,z,t), \tilde{\phi}(y,z,t), \tilde{p}(y,z,t))$ are shown to satisfy the adjoint equations

$$\left[\frac{\partial}{\partial\tau}-\mathrm{i}\alpha U_B\right]\tilde{u}-\frac{1}{Re}\left[\frac{\partial^2}{\partial z^2}+\frac{\partial^2}{\partial y^2}-\alpha^2\right]\tilde{u}+N\tilde{u}-\mathrm{i}\alpha\tilde{p}-\frac{\partial\tilde{\phi}}{\partial y}=0, \tag{4.11}$$

$$\left[\frac{\partial}{\partial\tau}-\mathrm{i}\alpha U_B\right]\tilde{v}-\frac{1}{Re}\left[\frac{\partial^2}{\partial z^2}+\frac{\partial^2}{\partial y^2}-\alpha^2\right]\tilde{v}+\frac{\partial U_B}{\partial y}\tilde{u}+N\tilde{v}-\frac{\partial\tilde{p}}{\partial y}+\mathrm{i}\alpha\tilde{\phi}=0, \tag{4.12}$$

$$\left[\frac{\partial}{\partial\tau}-\mathrm{i}\alpha U_B\right]\tilde{w}-\frac{1}{Re}\left[\frac{\partial^2}{\partial z^2}+\frac{\partial^2}{\partial y^2}-\alpha^2\right]\tilde{w}+\frac{\partial U_B}{\partial z}\tilde{u}-\frac{\partial\tilde{p}}{\partial z}=0, \tag{4.13}$$

$$\mathrm{i}\alpha\tilde{u}+\frac{\partial\tilde{v}}{\partial y}+\frac{\partial\tilde{w}}{\partial z}=0, \tag{4.14}$$

$$\left[\frac{\partial^2}{\partial z^2}+\frac{\partial^2}{\partial y^2}-\alpha^2\right]\tilde{\phi}-N\frac{\partial\tilde{u}}{\partial y}+\mathrm{i}\alpha N\tilde{v}=0 \tag{4.15}$$

with the boundary conditions

$$\tilde{u}=\tilde{v}=\tilde{w}=0, \quad \frac{\partial\tilde{\phi}}{\partial z}=0 \quad \text{at } z=\pm d/(2L), \tag{4.16}$$

$$\tilde{u}=\tilde{v}=\tilde{w}=0, \quad \frac{\partial\tilde{\phi}}{\partial y}=0 \quad \text{at } y=\pm a/(2L). \tag{4.17}$$

One obtains the optimal perturbation for time T by an iterative scheme, which is schematically illustrated by a diagram,

$$\left.\begin{array}{ccc} \boldsymbol{u}(y,z,0) & \overset{\text{Direct}}{\longrightarrow} & \boldsymbol{u}(y,z,T), \\ \uparrow & & \downarrow \\ \tilde{\boldsymbol{u}}(y,z,0) & \overset{\text{Adjoint}}{\longleftarrow} & \tilde{\boldsymbol{u}}(y,z,T). \end{array}\right\} \tag{4.18}$$

First, one propagates a given initial condition forward in time using the direct problem. This result serves as an 'initial' condition for the backward propagation by the adjoint equations:

$$\tilde{u}(y,z,T)=u(y,z,T), \quad \tilde{v}(y,z,T)=v(y,z,T), \quad \tilde{w}(y,z,T)=w(y,z,T). \tag{4.19}$$

After the backward propagation another relation between the direct and adjoined variables at $t=0$ is imposed:

$$\tilde{u}(y,z,0)=\frac{1}{\gamma}u(y,z,0), \quad \tilde{v}(y,z,0)=\frac{1}{\gamma}v(y,z,0), \quad \tilde{w}(y,z,0)=\frac{1}{\gamma}w(y,z,0). \tag{4.20}$$

An updated initial condition for the next iterative step is then available. This process should be self-consistent: convergence is reached when the initial condition for the forward problem does not change appreciably – up to a normalization constant – by an appropriately chosen criterion from one iterative step to the next. Finally, the maximum energy amplification is computed by propagating the converged initial condition once more in time and by forming the ratio of the disturbance energy at the end of the time interval to the energy at the beginning. The derivation of the adjoint equations and the iteration procedure is analogous to that for the channel flow presented in Krasnov *et al.* (2008). Some other particulars on the mathematical formulation can be found in the general reference Schmid & Henningson (2001).

The iterative method computes the maximum energy amplification $\hat{G}(\alpha, T, Re, Ha, r)$ as well as the structure of the optimal perturbation associated with a specific wavenumber α for given parameters T, Ha, Re, r. The function $\hat{G}$ can be maximized over wavenumbers α, thereby providing the maximum amplification $\hat{M}_{tot}(T, Re, Ha, r)$ among all the perturbations at given time T and flow parameters. This maximum amplification is reached at a particular wavenumber $\alpha_{tot}(T, Re, Ha, r)$. Further maximization over time T gives the global maximum amplification $M_{opt}(Re, Ha, r)$, which is reached at time $T=T_{opt}(Re, Ha, r)$. The corresponding optimal wavenumber is denoted by $\alpha_{opt}(Re, Ha, r)$. For purely streamwise perturbations, one defines the equivalent quantities $\hat{M}_{stream}(T, Re, Ha, r)\equiv\hat{G}(\alpha=0, T, Re, Ha, r)$ and $M_{stream}(Re, Ha, r)$.

5. Numerical method and verification

The base flow, direct and adjoint equations ((3.1)–(3.4), (4.3)–(4.9) and (4.11)–(4.17) respectively) are solved with a finite-difference approximation of second order on the rectangular duct cross-section. We use a collocated grid arrangement with velocity, electric current, pressure and electric potential defined at the same grid points. The grid is orthogonal and non-uniform. It is stretched in the wall-normal y and z directions to provide necessary refinement near the walls. This is done by applying transformations based on hyperbolic functions,

$$y = \frac{a}{2L}\,\frac{\tanh(\zeta_y \eta)}{\tanh(\zeta_y)}, \qquad z = \frac{d}{2L}\,\frac{\tanh(\zeta_z \theta)}{\tanh(\zeta_z)}, \tag{5.1}$$

in which coefficients ζ_y and ζ_z determine the grid stretching.

The problem is discretized on a uniform grid $[-1, 1] \times [-1, 1]$ in the variables (η, θ). Computations are performed on a grid consisting of up to 82 points in the direction of the shorter side of the duct and up to 288 points in the direction of the longer side. The grid size is modified in accordance with the values of r and Ha. The grid stretching parameters ζ_y and ζ_z vary between 1 and 2, so as to maintain the resolution of each boundary layer to no less than 12 grid points.

The operators grad(p), grad(ϕ) and div($\boldsymbol{u}$) as well as the velocity gradients in the convective term are expressed in terms of partial derivatives with respect to η and θ and are thereafter discretized in the interior domain using standard central differences of second order. Similarly, the viscous term $\Delta u/Re$ is approximated with the standard five-point central difference operator, which provides second-order accuracy in the interior. For points near the walls, one-sided three-point formulae are applied, which are also second-order accurate.

For time stepping, the standard explicit projection method with second-order Adams–Bashforth scheme is used. First, the intermediate non-solenoidal velocity field $\boldsymbol{u}^*$ is computed:

$$\frac{3\boldsymbol{u}^* - 4u^n + u^{n-1}}{2\delta t} = 2\boldsymbol{R}^n - \boldsymbol{R}^{n-1}, \tag{5.2}$$

where $\boldsymbol{R}^n$ and $\boldsymbol{R}^{n-1}$ stand for the sum of nonlinear, viscous and Lorentz force terms. The solenoidal velocity field $\boldsymbol{u}^{n+1}$ is then obtained through correction

$$\boldsymbol{u}^{n+1} = \boldsymbol{u}^* - \tfrac{2}{3}\Delta t\, \nabla\, p^{n+1}. \tag{5.3}$$

Pressure and electric potential fields are obtained via the Poisson equations

$$\nabla^2 p^{n+1} = \frac{3}{2\Delta t}\,\nabla \cdot \boldsymbol{u}^* \tag{5.4}$$

and

$$\nabla^2 \phi^{n+1} = \nabla \cdot (\boldsymbol{u}^{n+1} \times \boldsymbol{e}). \tag{5.5}$$

The electric potential satisfies the Neumann boundary conditions (see (4.8)–(4.9) and (4.16)–(4.17)). For the pressure field, the appropriate boundary conditions are found by projecting the correction equation (5.3) on the wall-normal direction:

$$\frac{\partial p^{n+1}}{\partial n} = \frac{3}{2\Delta t}\boldsymbol{u}_n^*. \tag{5.6}$$

These Poisson equations were solved by a direct solver from the FISHPACK libraries (Adams, Swarztrauber & Sweet 1999) providing a second-order finite-difference approximation with a standard five-point stencil for a two-dimensional rectangular

domain. Alternatively a multigrid iterative second-order solver from the MUDPACK libraries (Adams 1999) was also used. Both solvers have been checked for several reference problems. For the MUDPACK solver, three or four multigrid cycles per time step are sufficient to obtain a fully converged solution.

The base flow was computed by an iterative procedure. During each iteration, a Poisson equation was solved, in which the right-hand sides of (3.1) for U_B and (3.2) for ϕ_B were replaced by the value computed using the fields obtained from the previous iteration. These Poisson equations were discretized using the same grid, coordinate transformation and the second-order finite-difference approximation as the optimal perturbation equations. The converged solution has been verified through comparison with the infinite-series representation (see Müller & Bühler 2001).

Finally, the accuracy of the procedure (4.18) to get the optimal perturbations is secured by conducting a sufficiently large number of iterations. In all cases, at least 20 iterations are performed, after which the relative error $\|G^{(k+1)} - G^{(k)}\|/G^{(k)}$ is computed, where $G^{(k)}$ denotes the maximum amplification factor obtained at iteration k. If the error is smaller than 10^{-8}, the iterations are stopped. Typically, the number of iterations needed to achieve this criterion varied in the limits of $[50 \ldots 100]$, depending on the grid size, aspect ratio r and Hartmann number Ha.

We have verified our numerical code for several cases. The first test case is pure hydrodynamic ($Ha = 0$) duct flow with different aspect ratios. For this case, we have reproduced the flow patterns shown in figure 2 of Galletti & Bottaro (2004). We have also reproduced the flow structures and the values of amplification factor G obtained by D. Biau (personal communication, September 2009) for a square duct at $Re = 1000$ to within 1 %. The second test case is MHD channel flow. For this case the boundary conditions were changed to periodic in the y direction. We have reproduced the linear optimal growth results for the Hartmann flow (Gerard-Varet 2002; Krasnov *et al.* 2004) and for the Poiseuille flow under spanwise magnetic field (Krasnov *et al.* 2008).

6. Results

The numerical investigation of transient growth of linear perturbations has been conducted for $Ha = 0$, 10, 30 and 50 and $Re = 5000$. This Reynolds number is below the exponential instability limit $Re = 5772$ for plane Poiseuille flow and for a pure hydrodynamic duct flow of arbitrary cross-section (see Tatsumi & Yoshimura 1990). For a duct flow with a magnetic field, there are no results for the normal-mode instability. Our computations give no indication that exponential instability is present for this Reynolds number.

The analysis includes the streamwise perturbations ($\alpha = 0$) as well as perturbations with $\alpha \neq 0$. The investigated range of wavenumber α extends from 0 to 6, which has been found sufficient to capture the global maximum. The maximum range of time T is 200 for $0 \leqslant Ha \leqslant 10$ and 70 at $Ha = 30$ and $Ha = 50$. The optimal values of α and T corresponding to the maximum amplification are determined to an accuracy of 0.01 and 1, respectively.

In figure 5, the global maximum amplification $M_{tot}(Re, Ha, r)$ and the maximum amplification of streamwise perturbations $M_{stream}(Re, Ha, r)$ are shown as functions of Ha and r. Transient growth is present in all cases but is strongly suppressed by an imposed magnetic field. This is true for both types of perturbations and for all aspect ratios. The obvious explanation of such a suppression is the reduction by the Joule dissipation of perturbation kinetic energy. Remarkably, the maximum amplification

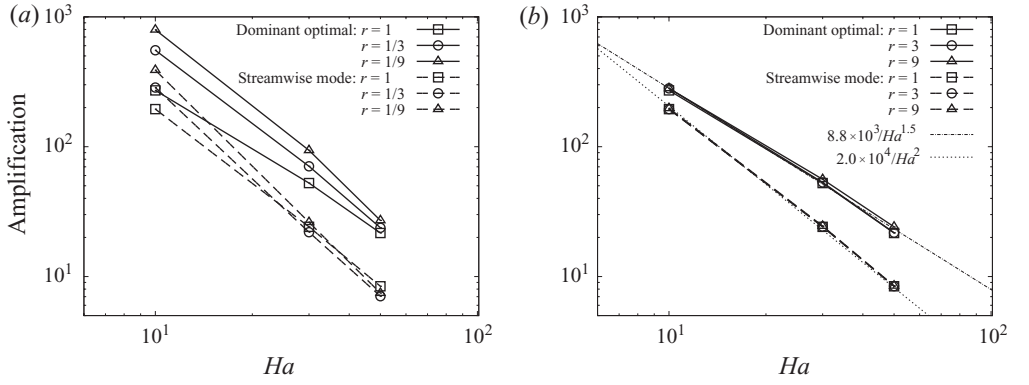

FIGURE 5. Global maximum amplification $M_{tot}(Re, Ha, r)$ (bold line) and maximum amplification of streamwise perturbations $M_{stream}(Re, Ha, r)$ (dashed line) are shown at $Re = 5000$ for different Hartmann numbers Ha and different aspect ratios r. The spanwise case $r \leqslant 1$ is presented in (a) and the Hartmann case $r \geqslant 1$ in (b).

is insensitive to the aspect ratio in the Hartmann case $r \geqslant 1$. This feature will receive an explanation in the discussion below.

6.1. *Results for square duct* $r = 1$

The amplification factors for arbitrary and purely streamwise perturbations are presented in figure 6. The curves for the case $Ha = 0$ (figure 6a) reproduce the results obtained by Biau *et al.* (2008) for smaller Reynolds number. The strongest amplification is due to the streamwise perturbations, except for small times T. Similar to the findings of Biau *et al.* (2008), the optimal streamwise modes have the form of four centrally symmetric rolls at smaller T (the first peak in figure 6a) and the form of two diagonally symmetric rolls at larger T (the second peak). Both peaks provide an almost identical level of amplification M_{stream}. Similar behaviour, when one streamwise optimal mode is taken over by another one, is also observed for the magnetic case. In particular, for $Ha = 10$ (figure 6b), the discontinuities of the slope of the amplification curves correspond to changes of optimal modes at $T \approx 15$ and $T \approx 50$. This effect is, however, much less pronounced than in the non-magnetic case (e.g. $Ha = 0$ versus $Ha = 10$) and almost disappears for stronger magnetic field ($Ha = 30$ and 50 in figure 6c, d).

At non-zero magnetic field, streamwise perturbations experience stronger Joule dissipation and stronger suppression than perturbations with $\alpha \neq 0$. At Hartmann numbers larger than a certain critical value (between 0 and 10) the strongest transient growth is provided by non-streamwise perturbations. Similar effects were observed by Krasnov *et al.* (2008) for channel flow with spanwise magnetic field. For all Hartmann numbers considered in our analysis, the streamwise modes return to being dominant at large T, but for much lower amplification.

The typical spatial structure of the optimal perturbations is illustrated in figure 7 for the streamwise case and in figure 8 for the global optimum with $\alpha \neq 0$. For non-zero magnetic field the perturbations become localized within the sidewall (Shercliff) boundary layers. Comparing figures 7(a) (respectively figure 7b) with figure 7(c) (respectively figure 7d) and the left and right panels of figure 8, we clearly see that by increasing the Hartmann number the optimal perturbations are more concentrated near the sidewalls in the increasingly thinner Shercliff layers.

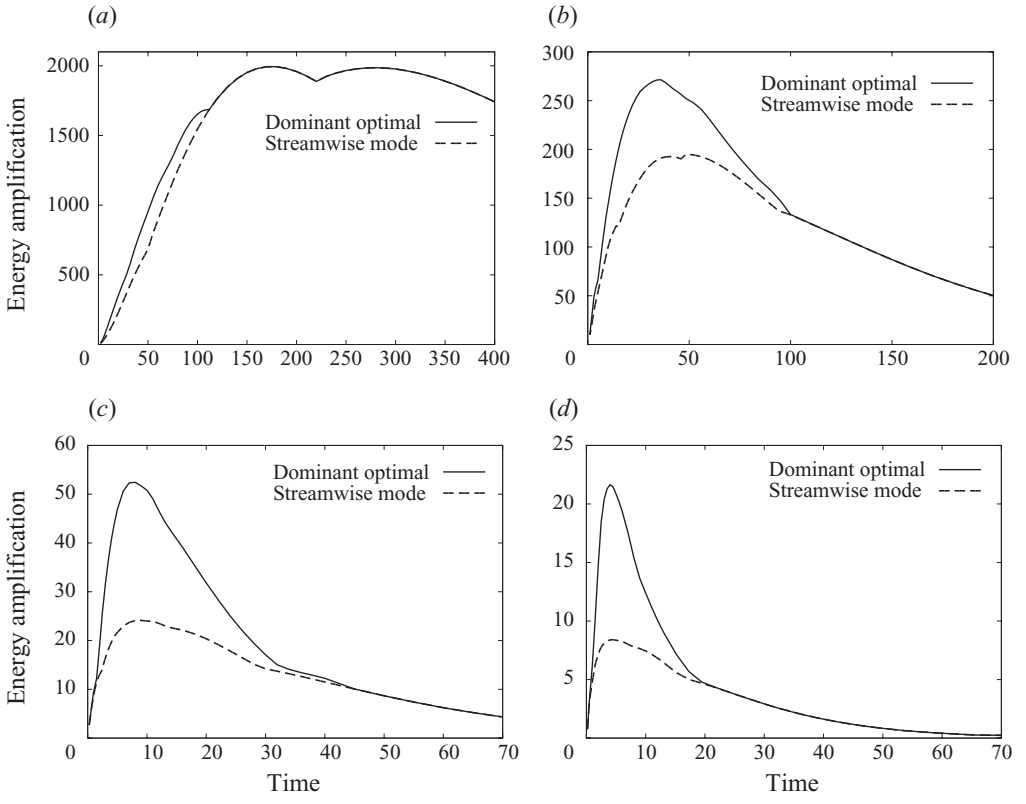

FIGURE 6. Case of square duct ($r = 1$). Energy amplification factors $\hat{M}_{tot}(T, Re, Ha, r)$ (———) and $\hat{M}_{stream}(T, Re, Ha, r)$ (– – – –) as a function of time T. The results are shown for $Re = 5000$ and various Hartmann numbers: (a) $Ha = 0$, (b) $Ha = 10$, (c) $Ha = 30$, (d) $Ha = 50$.

For the optimal streamwise perturbations, the internal structure and evolution are, in their principal features, similar to non-magnetic, parallel shear flows, such as channel or pipe flow. The only apparent difference is that optimal streamwise perturbations in the MHD duct are strongly concentrated in the Shercliff layers as mentioned above. The initial form of the optimal streamwise perturbations is that of streamwise rolls (cf. figure 7a, c). The evolution is dominated by the lift-up mechanism, which leads to development of streamwise streaks of low and high streamwise velocity (cf. figure 7b, d). The transformation from rolls to streaks can be quantified by the distribution of perturbation energy among velocity components. At $t = 0$, the energy is almost entirely in the components v_y and v_z. The streamwise component v_x contains about 0.1 % of total energy at $Ha = 10$ and about 2.5 % at $Ha = 50$. At the time T_{opt} of maximum amplification, the streamwise velocity component invariably contains more than 99 % of the total perturbation energy.

The patterns of optimal perturbations with $\alpha \neq 0$ are significantly more complex, although they can be presented in terms of roll-like and streak-like structures. The 'rolls' at $t = 0$ are visible in figure 8(a,b), while the streaks that have evolved by T_{opt} are illustrated in figure 8(c–f). The main difference with the streamwise perturbations is that the structures are inhomogeneous in the x direction and form complex overlapping patterns within the Shercliff boundary layers. The distribution of perturbation energy among the velocity components varies with Ha. In the initial

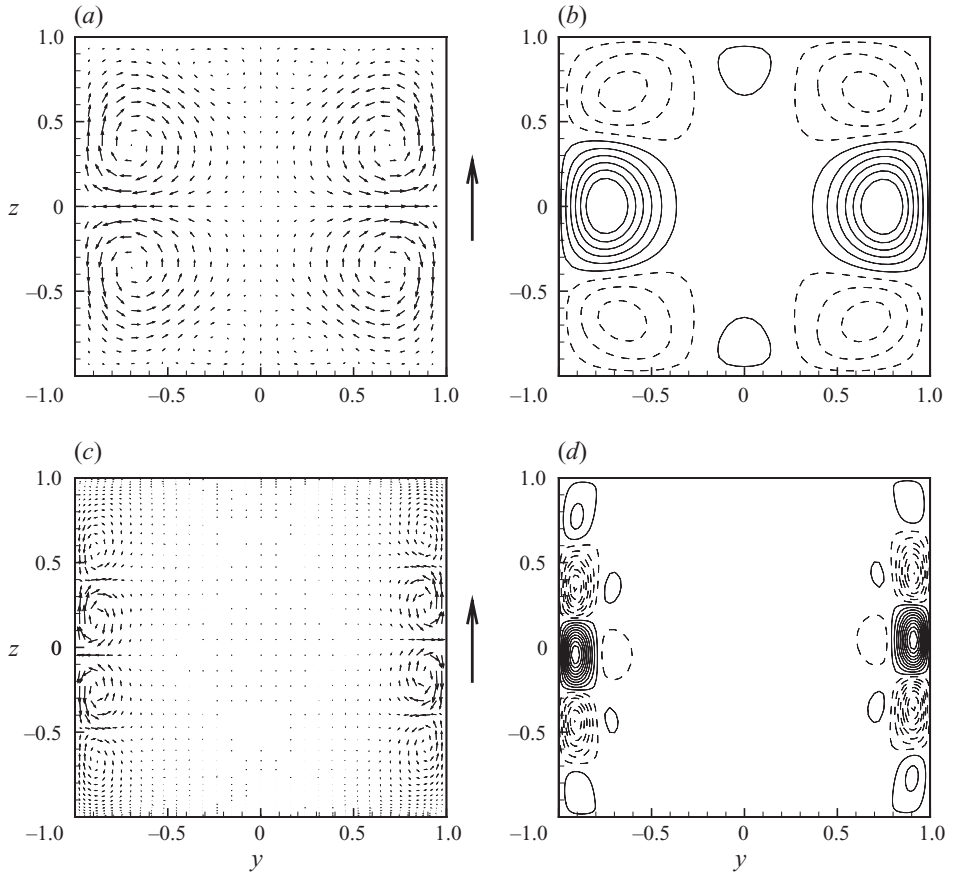

FIGURE 7. Case of square duct ($r = 1$): the streamwise optimal perturbation which generates the maximum amplification $M_{stream}(Re, Ha, r = 1)$ for Reynolds number $Re = 5000$ and Hartmann numbers (*a*, *b*) $Ha = 10$ and (*c*, *d*) $Ha = 50$. The optimal perturbations at $t = 0$ are shown in (*a*) and (*c*) using the velocity vectors projected on to the duct cross-section. In (*b*) and (*d*) the isolines of streamwise velocity perturbation for the optimal perturbations are displayed at time T_{opt} of largest amplification. The solid and dashed lines in (*b*) and (*d*) correspond to positive and negative values, and the arrow indicates the direction of the applied magnetic field.

state, v_x^2, v_y^2 and v_z^2 contain, respectively, 2 %, 15 % and 83 % of the total energy at $Ha = 10$ and 15 %, 4 % and 81 % at $Ha = 50$. In the state of maximum amplification at T_{opt}, the distribution changes to 98 %, 0.2 % and 1.8 % at $Ha = 10$ and to 82 %, 1.2 % and 16 % at $Ha = 50$. The data at T_{opt} are particularly interesting. If one identifies streaks with the dominance of the streamwise velocity components, we conclude that the streak-like structures dominate the optimal perturbations (strongly at $Ha = 10$ and less so at $Ha = 50$) even in the general (non-streamwise) case.

The non-streamwise perturbations in figure 8 are closely related to the oblique optimal perturbations observed by Krasnov *et al.* (2008) in the channel with spanwise magnetic field. The only apparent difference is that the confinement by the Hartmann walls in the duct precludes periodicity in the z direction and thereby the existence of perturbations with parallel isolines that are inclined with respect to the x–y plane. The structures in figure 8 strongly resemble those obtained in the channel with spanwise field by superposition of symmetric modes with the same streamwise wavenumbers α and spanwise z wavenumbers with equal magnitude and opposite sign.

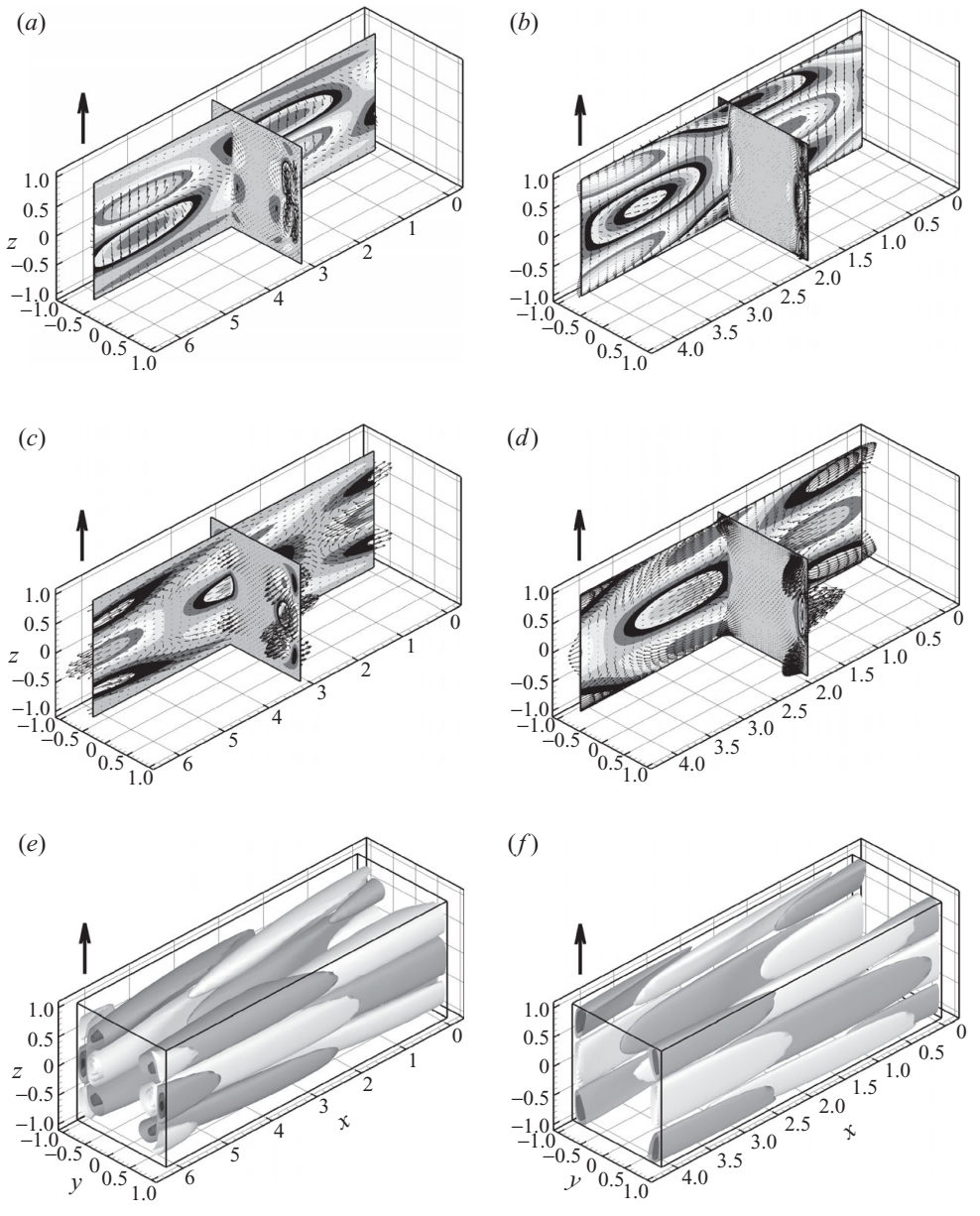

FIGURE 8. Case of square duct ($r = 1$): the optimal perturbations corresponding to the maximum amplification $M_{opt}(Re, Ha, r)$ are displayed for Reynolds number $Re = 5000$ and Hartmann numbers (a, c, e) $Ha = 10$ and (b, d, f) $Ha = 50$. Vector plots together with isocontours of the streamwise velocity are shown in the two-dimensional cuts (a, b) at $t = 0$ and (c, d) at T_{opt}. Isosurfaces of the streamwise velocity v_x at T_{opt} are also shown in (e) and (f). The arrow indicates the orientation of the applied magnetic field.

6.2. *Spanwise case* $r < 1$

The results for ducts elongated in the direction of the magnetic field will be compared with the square duct and with the channel with spanwise magnetic field (Krasnov *et al.* 2008). The amplification factors $\hat{M}_{tot}(T, Re, Ha, r)$ and the corresponding

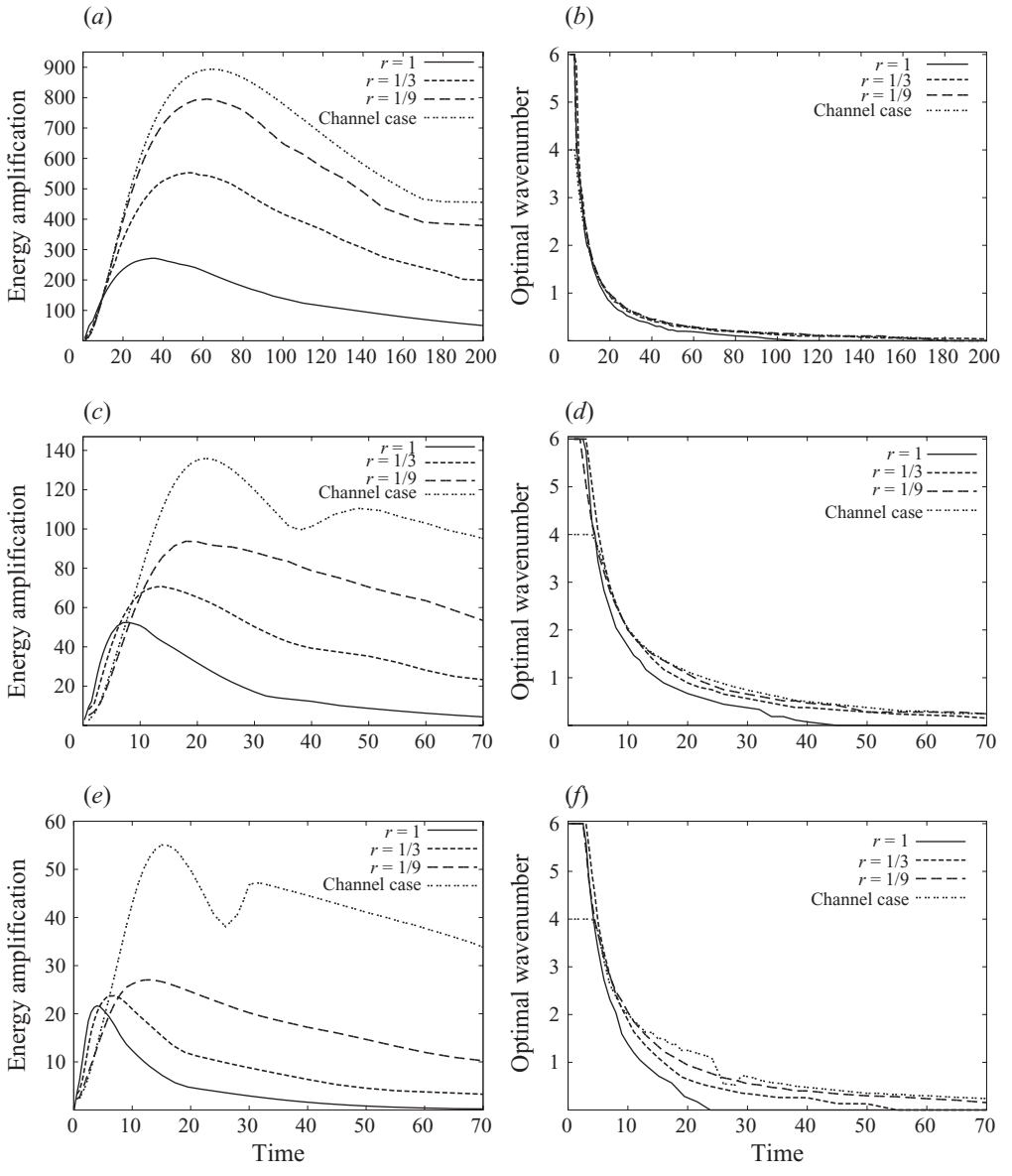

FIGURE 9. Transient growth for the spanwise case ($r < 1$). Data for $r = 1$ and for a channel with spanwise magnetic field (Krasnov *et al.* 2008) are included for comparison. (*a*, *c*, *e*) Energy amplification factors $\hat{M}_{tot}(T, Re, Ha, r)$ and (*b*, *d*, *f*) the corresponding optimal wavenumbers $\alpha_{tot}(T, Re, Ha, r)$ are shown as functions of T for $Re = 5000$ and $Ha = (a,b)$ 10, (c,d) 30 and (e,f) 50.

wavenumbers $\alpha_{tot}(T, Re, Ha, r)$ are shown in figure 9. For all r and Ha considered, the strongest growth is provided by perturbations with $\alpha \neq 0$. The optimal wavenumber α_{tot} is monotonically decreasing with T. For small T it starts at large values exceeding the limit $\alpha = 6$ of our wavenumber range. An increase of Ha at a fixed r consistently leads to lower amplifications, to a shift of the optimal time T_{opt} to smaller values and finally to an increase of the optimal wavenumber α_{opt} (this can be seen, e.g., in figure 8). Conversely, decreasing r from 1 to 1/9 at fixed Hartmann number Ha leads

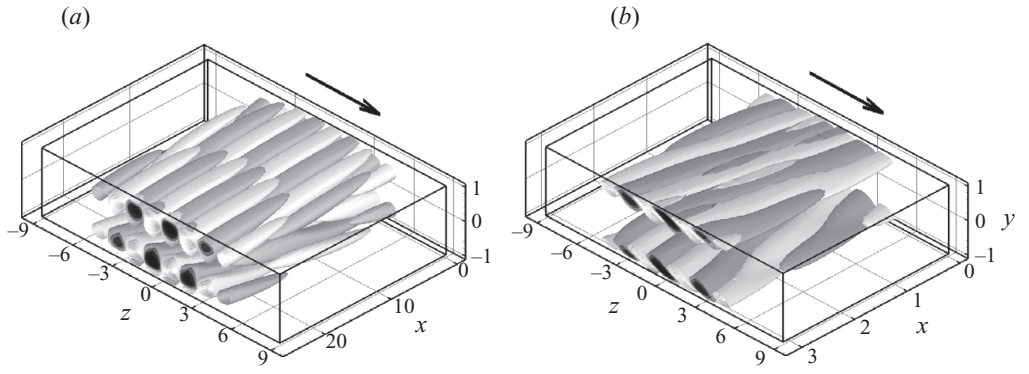

FIGURE 10. Spanwise case ($r = 1/9$). The optimal perturbation at T_{opt} corresponding to maximum amplification $M_{opt}(Re, Ha, r)$ is shown using isosurfaces of the streamwise velocity perturbation for Reynolds number $Re = 5000$ and Hartmann numbers (*a*) $Ha = 10$ and (*b*) $Ha = 50$. The arrow indicates the orientation of the applied magnetic field.

to an increase of the maximum amplification M_{opt}, to a shift of the optimal time T_{opt} to larger values and to a reduction of the global optimal wavenumber α_{opt}. The change in M_{opt} is significant at $Ha = 10$ (about fourfold), less significant at $Ha = 30$ and even less so at $Ha = 50$.

The spatial structure of the global optimal perturbation is illustrated in figure 10 using isosurfaces of the streamwise velocity. As for the square duct (cf. figure 8*e*, *f*) the perturbations have the form of non-streamwise streaks at the time of strongest amplification. They occupy most of the Shercliff layers if one ignores the corners.

All plots in figure 9 demonstrate that the duct results tend towards the curves for the channel with spanwise magnetic field as r decreases. This is true for the general shape of the curves as well as for their quantitative characteristics, namely the global maximum amplification, the time T_{opt} and the optimal wavenumber α_{opt}. For $r = 1/9$, convergence to the channel case is almost achieved at $Ha = 10$. For $Ha = 30$ and $Ha = 50$, one evidently needs lower aspect ratios than the minimum $r = 1/9$ used in our computations. In the hydrodynamic case, an aspect ratio of $r \sim 1/6$ is sufficient as shown by Galletti & Bottaro (2004).

The behaviour with decreasing r can be explained by the structure of the optimal perturbations. As for the square duct, the structure of the perturbations is analogous to that of the oblique perturbations, which dominate in the channel with spanwise field. When decreasing r while keeping Ha fixed, the optimal perturbations residing in the Shercliff layers experience a weaker lateral confinement. One thereby approaches the channel in terms of geometry.

The deviation between the channel and the duct with fixed $r < 1$ is increasing with increasing Ha. This can be explained by differences in the basic velocity distributions between the duct and the channel. For the duct, the relevant parts are the Shercliff layers, which scale as $\delta_{Sh} \approx a r^{-1/2} Ha^{-1/2}$. By contrast, the channel base flow is insensitive to the magnetic field and is characterized by a parabolic Poiseuille profile.

6.3. *Hartmann case* $r > 1$

For aspect ratios $r > 1$, the shorter walls of the duct are parallel to the magnetic field. Curves of maximum amplification and optimal wavenumbers are shown in figure 11. General tendencies are the same as for the spanwise case (cf. figure 9): perturbations

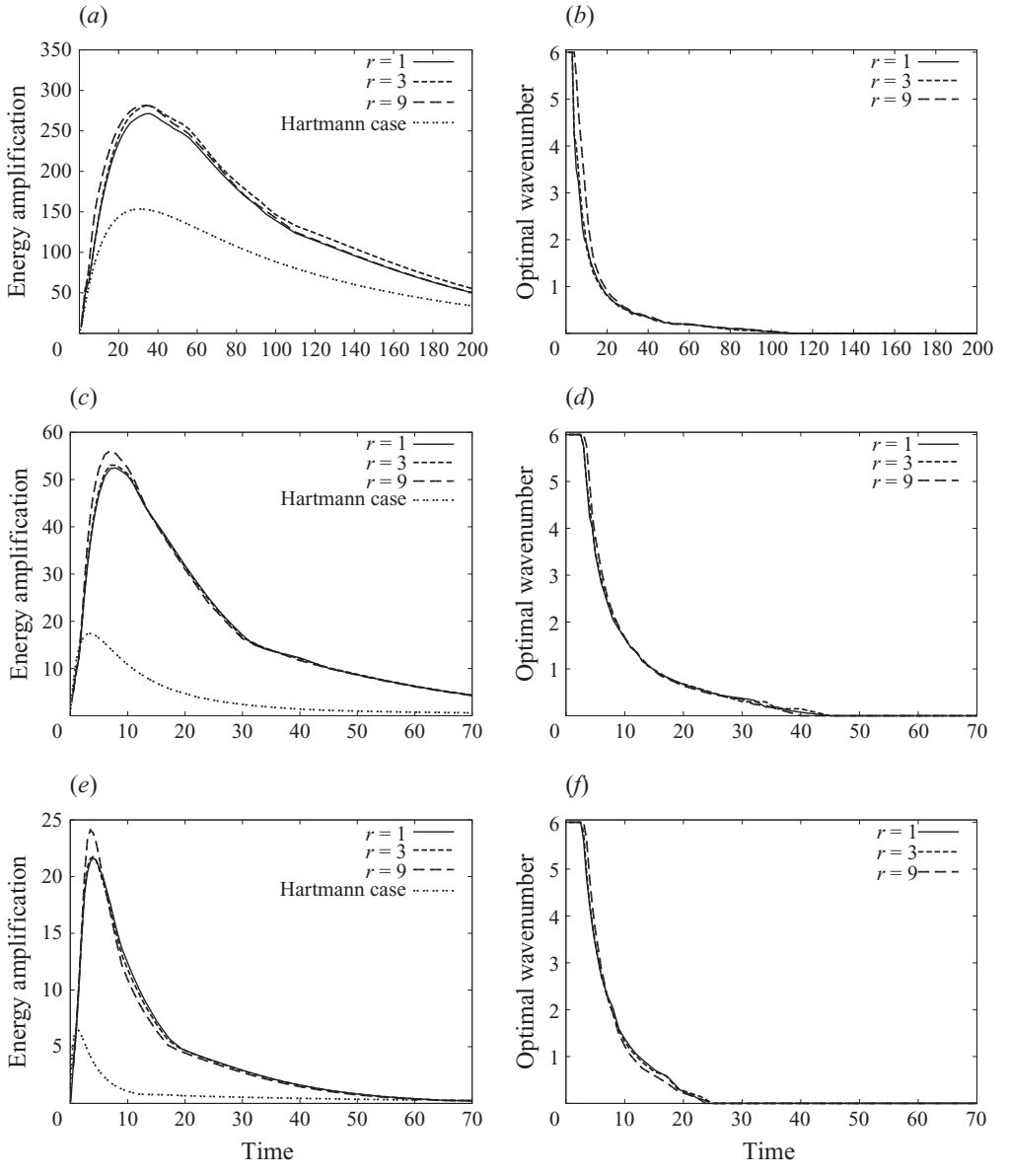

FIGURE 11. Transient growth for the Hartmann case $r > 1$. Data for the square duct $r = 1$ and for the Hartmann channel are included for comparison. Energy amplification factors (a, c, e) $\hat{M}_{tot}(T, Re, Ha, r)$ and the corresponding optimal wavenumbers (b, d, f) $\alpha_{tot}(T, Re, Ha, r)$ are shown as functions of T for $Re = 5000$ and $Ha =$ (a,b) 10, (c,d) 30 and (e,f) 50.

with $\alpha \neq 0$ dominate, although the optimal α_{tot} decreases with T. Likewise, increasing Ha leads to a significant reduction of the amplification and to a shift of the global maximum towards smaller times.

A major difference between figures 9 and 11 is in the effect of the aspect ratio r. In contrast with the spanwise case $r < 1$, the amplification rates and optimal wavenumbers are virtually insensitive to r at $r \geqslant 1$. Furthermore, the results show no tendency of converging towards the results for the Hartmann channel. This is true

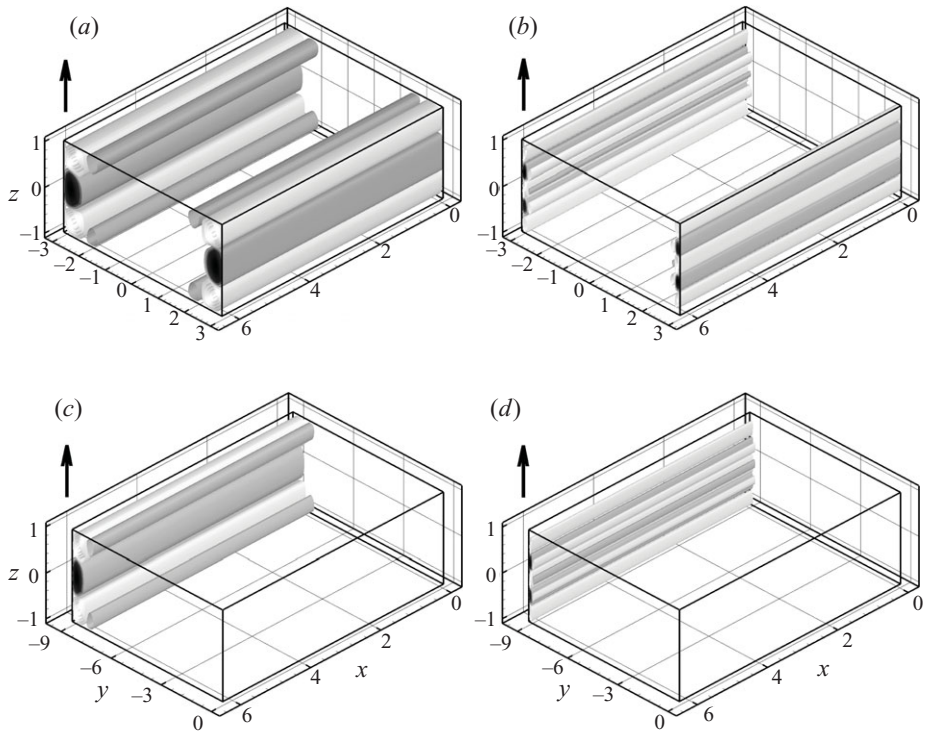

FIGURE 12. Hartmann case ($r > 1$). The streamwise optimal modes, which generate the maximum amplification $M_{stream}(Re, Ha, r)$, for Reynolds number $Re = 5000$ and Hartmann numbers (a, c) $Ha = 10$ and (b, d) $Ha = 50$. Spatial structure at T_{opt} is shown by isosurfaces of the streamwise velocity for (a, b) $r = 3$ and (c, d) $r = 9$. Note that for $r = 9$, only one half of the domain is shown. The arrow indicates the orientation of the applied magnetic field.

for the amplification curves (as illustrated in figure 11*a*, *c*, *e*) and for the optimal wavenumbers α_{opt} (the optimal perturbations in the Hartmann channel are purely streamwise). The reason for such a behaviour becomes clear when we consider the structure of the optimal perturbations at $r > 1$. It is illustrated in figures 12 and 13 using the isosurfaces of the streamwise velocity at $t = T_{opt}$. One can see that the perturbations are invariably localized within the Shercliff boundary layers. This is true for all values of r and Ha considered in our study. The global optimal perturbations shown in figure 13 have a structure similar to that of the global optimal perturbations observed at $r = 1$ and $r < 1$ (cf. figures 8*e*, *f* and 10). As illustrated in figure 12, even the streamwise perturbations do not reproduce the behaviour of the streamwise perturbations in the channel case. Rather, they are localized within the Shercliff layers. For both kinds of perturbations, the localization within the Shercliff layers means that increasing r, i.e. extending the duct in the y direction, does not affect their development. This invariance with respect to r also relies on the convergence of the basic velocity distribution near the sidewalls, which is demonstrated in figure 4(*b*, *d*).

In addition, the basic velocity distribution within the Shercliff layer also becomes approximately one-dimensional with a universal shape when it is scaled with δ_{Sh}. Because of this property, one can take the analysis of streamwise perturbations one step further and look for scaling behaviour with respect to Ha. The basic idea is to consider a single Shercliff layer in isolation and to neglect the Hartmann walls. One

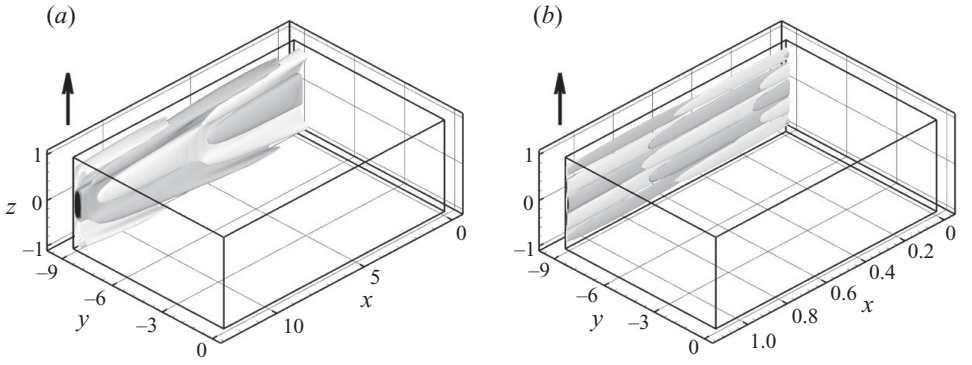

FIGURE 13. Hartmann case ($r = 9$). The optimal mode corresponding to the maximum amplification $M_{opt}(Re, Ha, r)$ for Reynolds number $Re = 5000$ and Hartmann numbers (*a*) $Ha = 10$ and (*b*) $Ha = 50$. Spatial structure at T_{opt} is shown by isosurfaces of the streamwise velocity in one half of the domain. The arrow indicates the orientation of the applied magnetic field.

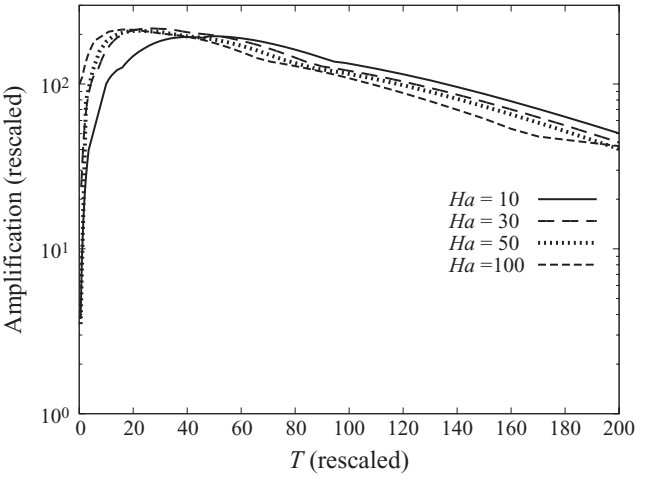

FIGURE 14. Rescaled amplification factor GHa^2 as a function of rescaled time THa for streamwise optimal perturbations. Results for the square duct $r = 1$ are shown for $Re = 5000$ and $Ha = 10$, 30, 50 and 100.

thereby arrives at a configuration resembling channel flow with spanwise magnetic field, except that the basic velocity distribution is that of the Shercliff layer and not a parabolic profile. The length scale δ_{Sh} of the basic velocity distribution depends on Ha. Consequently, the arguments for the scaling of streamwise perturbations given by Krasnov *et al.* (2008) for channel flow have to be modified slightly. Details are given in the Appendix. The analysis provides the scaling

$$\hat{G}(\alpha = 0, T, Re, Ha, r) = \left(\frac{Re}{Ha}\right)^2 \mathscr{G}(THa/Re) \tag{6.1}$$

for streamwise optimal perturbations, where $\mathscr{G}$ is a universal function. Figure 14 shows that, as predicted by (6.1), the amplification curves at different values of Ha follow each other closely when normalized with $(Ha/Re)^2$ (amplification) and Re/Ha (time). The scaling (6.1) also satisfies the Ha^{-2} decay of the amplification of

streamwise perturbations in figure 5(*b*). However, these scaling arguments cannot be applied to non-streamwise perturbations. We cannot provide a theoretical basis for the apparent $Ha^{-1.5}$ power law in figure 5(*b*).

7. Conclusions

We have analysed the optimal linear growth of perturbations in a duct flow with rectangular cross-section and uniform, transverse magnetic field aligned with one pair of walls.

The disturbances with the strongest amplification reside in the Shercliff layers. Purely streamwise perturbations experience a strong suppression by the magnetic field. They cease to be the most amplified perturbations at fairly low values of Ha and are replaced by perturbations with a non-zero streamwise wavenumber on account of a weaker damping by the magnetic field as discussed by Krasnov *et al.* (2008) for the MHD channel flow. These observations apply irrespective of the aspect ratio r.

When the Shercliff layers overlap at sufficiently low r, the basic velocity profile across these layers approaches the parabolic Poiseuille profile. In this case, the results for MHD channel flow with spanwise field are recovered in MHD duct flow. The required values for r should be of order $r \sim 1/Ha$ because the width of the Shercliff layers scales as $\delta_{Sh} \approx ar^{-1/2}Ha^{-1/2}$. By contrast, the limit of large r fails to reproduce the results for Hartmann channel flow (with wall-normal magnetic field). In this latter configuration, sidewalls are not present by definition, and hence there are no Shercliff layers. In that instance, perturbations necessarily reside in the Hartmann layers.

The results for MHD duct flow at large r become independent of r on account of the invariance of the basic flow within the Shercliff layers. From this perspective, the MHD flow in a square duct captures all relevant aspects of the behaviour for larger r. In addition, one can apply scaling arguments to individual Shercliff layers and thereby recover a scaling of the amplification with Ha^{-2} at given Re found in MHD duct simulations.

The fundamental mechanism of transient amplification in the MHD duct flow appears to be the hydrodynamic lift-up mechanism for all parameter combinations of Re, Ha and r in our present investigation. This conclusion is based on the relative magnitude of velocity perturbation components at the beginning and the peak of transient amplification. In contrast with our previous channel flow study with spanwise field (Krasnov *et al.* 2008), the Hartmann walls preclude the existence of purely two-dimensional perturbations, which are uniform along the magnetic field. In the MHD channel with spanwise field, such perturbations provide transient amplification by the Tollmien–Schlichting mechanism and lead to a minimum amplification level irrespective of the magnitude of Ha. This effect is not seen in our present study. However, the Tollmien–Schlichting mechanism should in principle be capable of providing transient amplification in the MHD duct flow as well. To investigate this possibility one would have to consider significantly larger values of Re and Ha such that the Reynolds number based on the Shercliff layer thickness remains large for large interaction parameter Ha^2/Re. This assumption is made in the study by Potherat (2007), where the flow is averaged in the direction of the magnetic field at the outset.

Clearly, the next steps in the investigation of transition in MHD duct flow require nonlinear simulations. Our present stability code has been used as a basis for the development of a suitable direct numerical simulation code, which has already

been successfully validated for hydrodynamic duct flow and MHD channel flows. Preliminary simulations indicate that transition starts in the Shercliff layers as expected from the transient growth analysis. It would also be interesting to analyse the transient growth at larger Re and Ha. Although it is reasonable to believe that the key results of the present study, such as the concentration of the growth in Shercliff layers, are retained in a wide parameter range, some new features may appear.

We are grateful to André Thess for interesting discussions and useful comments, to Damien Biau for sharing his results for code verification, and to the organizers Bernard Knaepen and Daniele Carati of the MHD Summer Program 2009 at the Université Libre de Bruxelles, where this work was completed. T.B., D.K. and O.Z. acknowledge financial support from the Deutsche Forschungsgemeinschaft (Emmy–Noether grant Bo 1668/2-4 and Gerhard-Mercator visiting professorship programme). Computer resources were provided by the computing centre of TU Ilmenau.

Appendix. Scaling of streamwise perturbations

For purely streamwise perturbations, the two-dimensional basic velocity distribution in the Shercliff layers (close for instance to the wall at $y=-a/2$) is approximated by a one-dimensional profile $U(y,z)\approx U_0(y+a/2)$, where y is the coordinate perpendicular to the magnetic field.

Let us restart within a dimensional setting, and let us consider purely streamwise perturbations that are periodic in the z direction with dimensional wavenumber β:

$$v_i(y,t)\exp(\mathrm{i}\beta z),\quad p(y,t)\exp(\mathrm{i}\beta z),\quad \phi(y,t)\exp(\mathrm{i}\beta z). \tag{A 1}$$

The velocity v and vorticity ω_y component along the y direction (wall-normal direction) satisfy the dimensional equations that are obtained by taking the curl and twice the curl of the linearized Navier–Stokes equations and projecting on the y direction only:

$$\partial_t\frac{\omega_y}{\beta}=\nu\nabla^2\frac{\omega_y}{\beta}-\mathrm{i}v\mathrm{D}U_0-\mathrm{i}\frac{\sigma B_0}{\rho}\mathrm{D}\phi-\frac{B_0^2\sigma}{\rho}\frac{\omega_y}{\beta}, \tag{A 2}$$

$$\partial_t\nabla^2 v=\nu\nabla^4 v+\beta^2\frac{B_0^2\sigma}{\rho}v, \tag{A 3}$$

$$\nabla^2\phi=\mathrm{i}B_0\mathrm{D}\frac{\omega_y}{\beta}, \tag{A 4}$$

where $\mathrm{D}\equiv\partial_y$, $\nabla^2\equiv\mathrm{D}^2-\beta^2$ and

$$\eta=\frac{\omega_y}{\beta}=\mathrm{i}u \tag{A 5}$$

with u the streamwise velocity. The velocity w in the z direction is determined by the incompressibility:

$$\mathrm{D}v+\mathrm{i}\beta w=0. \tag{A 6}$$

Let us then eliminate the term with $\mathrm{D}\phi$ in (A 2) by taking the derivative D of (A 2) and using (A 4). The result is

$$\partial_t\mathrm{D}\eta=\nu\nabla^2\mathrm{D}\eta-\mathrm{i}\mathrm{D}\,(v\mathrm{D}U_0)-\mathrm{i}\frac{B_0^2\sigma}{\rho}\beta^2\phi. \tag{A 7}$$

The profile $U_0(y+a/2)$ attains a maximum value V at a distance δ from the wall. The quantity δ characterizes the width of the Shercliff layer. Let us non-dimensionalize

(A 3), (A 4) and (A 7) by choosing the following units:

$$\left.\begin{array}{l} [y]=\delta, \quad [\beta]=1/\delta, \quad [t]=\delta^2/\nu, \quad [U_0]=[\eta]=[u]=V, \\ [v]=[w]=\nu/\delta, \quad [\phi]=VB_0\delta. \end{array}\right\} \tag{A 8}$$

The dimensionless quantities are denoted by a tilde, e.g. $\tilde{y}=(y+a/2)/\delta$. The dimensionless equations are

$$\partial_{\tilde{t}}\tilde{\mathrm{D}}\tilde{\eta} = \tilde{\nabla}^2\tilde{D}\tilde{\eta} - \mathrm{i}\tilde{\mathrm{D}}\left(\tilde{v}\tilde{\mathrm{D}}\tilde{U}_0\right) - \mathrm{i}Ha_\delta^2\tilde{\beta}^2\tilde{\phi}, \tag{A 9}$$

$$\partial_{\tilde{t}}\tilde{\nabla}^2\tilde{v} = \tilde{\nabla}^4\tilde{v} + Ha_\delta^2\tilde{\beta}^2\tilde{v}, \tag{A 10}$$

$$\tilde{\nabla}^2\tilde{\phi} = \mathrm{i}\tilde{\mathrm{D}}\tilde{\eta}. \tag{A 11}$$

In these equations, the Hartmann number is based on δ:

$$Ha_\delta = B_0\delta\sqrt{\frac{\sigma}{\rho\nu}}. \tag{A 12}$$

When represented in units based on δ and V, the base velocity profile, i.e. $\tilde{U}_0(\tilde{y})$, is the same for different aspect ratios and Hartmann numbers. As a consequence, the above equations only depend on two dimensionless parameters, namely the wavenumber $\tilde{\beta}$ (in $\tilde{\nabla}^2$) and $Ha_\delta\tilde{\beta}$. Boundary conditions for the variables need to be imposed on the boundaries $\tilde{y}=0$ and $\tilde{y}=a/\delta$. However we assume here that the perturbations are vanishing away from the Shercliff layer so that a/δ can be replaced by ∞.

The dimensional kinetic energy of the perturbations integrated across the Shercliff layers thus reads

$$E(t) \equiv \int_0^{a/\delta} \left[|u|^2+|v|^2+|w|^2\right] \mathrm{d}y = \frac{\nu^2}{\delta}\frac{1}{\tilde{\beta}^2}\left(E_v(t)+\tilde{\beta}^2Re_\delta^2E_\eta(t)\right), \tag{A 13}$$

where

$$E_v(t) = \int_0^\infty \left(|\tilde{\mathrm{D}}\tilde{v}|^2+\tilde{\beta}^2|\tilde{v}|^2\right)\mathrm{d}\tilde{y} \quad \text{and} \quad E_\eta(t) = \int_0^\infty |\tilde{\eta}|^2\mathrm{d}\tilde{y} \tag{A 14}$$

and

$$Re_\delta = \frac{V\delta}{\nu} \tag{A 15}$$

stands for the Reynolds number based on the thickness of the Shercliff layer.

If we assume that the mechanism of ordinary hydrodynamics applies, in which the growth is due to the forcing of wall-normal vorticity by wall-normal velocity, the energy at $t=0$ is predominantly in the E_v term and, at maximum amplification, is predominantly in the E_η term. This imposes that the amplification at time t is equal to

$$G \equiv \mathrm{Max}\left(\frac{E(t)}{E(0)}\right) = \tilde{\beta}^2Re_\delta^2\tilde{G}(\tilde{t},\tilde{\beta}^2,\tilde{\beta}^2Ha_\delta^2), \tag{A 16}$$

where $\tilde{G}(\tilde{t},\tilde{\beta}^2,\tilde{\beta}^2Ha_\delta^2)$ is a function determined by an optimization problem: find the optimum perturbation in $\tilde{v}$, $\tilde{\eta}$ satisfying (A 9)–(A 11), which maximizes the ratio

$$\frac{E_\eta(\tilde{t})}{E_w(0)} \tag{A 17}$$

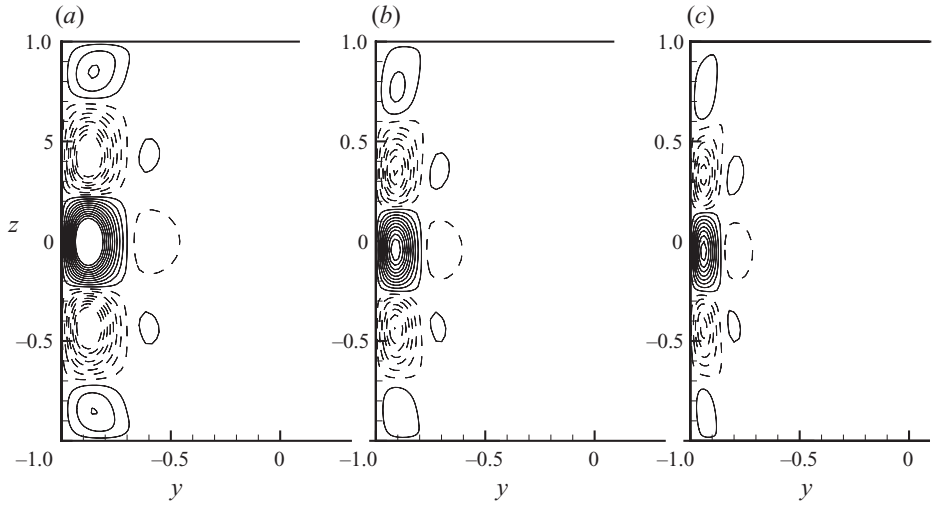

FIGURE 15. Streamwise optimal perturbations in the square duct for Reynolds number $Re = 5000$ and Hartmann numbers (*a*) $Ha = 30$, (*b*) $Ha = 50$ and (*c*) $Ha = 100$. The patterns are shown at time T_{opt} by the isolines of streamwise velocity perturbation u (only one half of the domain is visualized). Note that the 'virtual' wavenumber β (used in (A 1)) is considered along the z direction.

at $\tilde{t}$. Let us now assume that $\tilde{\beta}$ tends asymptotically to zero as Ha_δ grows. In that case,

$$G = Re_\delta^2 \tilde{\beta}^2 \tilde{H}\left(\tilde{t}, \tilde{\beta}^2 Ha_\delta^2\right) = \frac{Re_\delta^2}{Ha_\delta^2} \tilde{\beta}^2 Ha_\delta^2 \tilde{H}\left(\tilde{t}, \tilde{\beta}^2 Ha_\delta^2\right) = \frac{Re^2}{Ha^2} \tilde{\beta}^2 Ha_\delta^2 \tilde{H}\left(\tilde{t}, \tilde{\beta}^2 Ha_\delta^2\right),$$

where $H(\tilde{t}, R)$ is a function determined by a simplified optimization problem: find the optimum perturbation in $\tilde{v}$, $\tilde{\eta}$ satisfying equations depending on a unique coefficient R,

$$\partial_{\tilde{t}} \tilde{\mathrm{D}} \tilde{\eta} = \tilde{D}^3 \tilde{\eta} - \mathrm{i}\tilde{\mathrm{D}}\left(\tilde{v}\tilde{\mathrm{D}}\tilde{U}_0\right) - \mathrm{i}R\tilde{\phi}, \tag{A 18}$$

$$\partial_{\tilde{t}} \tilde{\mathrm{D}}^2 \tilde{v} = \tilde{\mathrm{D}}^4 \tilde{v} + R\tilde{v}, \tag{A 19}$$

$$\tilde{\mathrm{D}}^2 \tilde{\phi} = \mathrm{i}\tilde{\mathrm{D}}\tilde{\eta}, \tag{A 20}$$

which maximizes the ratio (A 17) at $\tilde{t}$. Figure 14 shows that this scaling is observed in our calculations, since it is easily seen that

$$\tilde{t} = t \frac{\nu}{\delta^2} \frac{L}{U_0} = t \frac{L^2}{\delta^2} \frac{1}{Re} = t \frac{Ha}{Re}$$

because the Shercliff layer scales with $\delta \approx L/Ha^{1/2}$.

Let us now assume that function $RH(\tilde{t}, R)$ possesses a global maximum at $R = R_c$ and $\tilde{t} = \tilde{t}_c$, which can be checked numerically. This is easily seen to imply the scalings

$$M_{stream} = \frac{Re^2}{Ha^2} R_c H(\tilde{t}_c, R_c), \tag{A 21}$$

$$\beta = \frac{L}{\delta}\tilde{\beta} = \frac{L}{\delta}\frac{\sqrt{R_c}}{Ha_\delta} = \sqrt{R_c} \quad \text{and} \quad T_{opt} = \frac{Re}{Ha}\tilde{t}_c, \tag{A 22}$$

which are well supported by the results in figure 14. They also account for the Ha scaling for M_{stream} in figure 5. Finally, figure 15 demonstrates that the number of

vortices in the Shercliff layers hardly changes with Ha; i.e. the effective wavenumber $\tilde{\beta}$ tends to zero with increasing Ha_δ, while the product $\tilde{\beta} Ha_\delta$ remains nearly constant.

REFERENCES

Adams, J. C. 1999 MUDPACK: multigrid software for elliptic partial differential equations. `http://www.cisl.ucar.edu/css/software/mudpack/`.

Adams, J. C., Swarztrauber, P. & Sweet, R. 1999 Efficient fortran subprograms for the solution of separable elliptic partial differential equations. `http://www.cisl.ucar.edu/css/software/fishpack/`.

Airiau, C. & Castets, M. 2004 On the amplification of small disturbances in a channel flow with a normal magnetic field. *Phys. Fluids* **16**, 2991–3005.

von Ammon, W., Gelfgat, Y., Gorbunov, L., Muhlbauer, A., Muiznieks, A., Makarov, Y., Virbulis, J. & Muller, G. 2005 Application of magnetic fields in industrial growth of silicon single crystals. In *The 15th Riga and 6th PAMIR Conference on Fundamental and Applied MHD Modeling of MHD Turbulence*, vol. I, pp. 41–54, Riga, Latvia.

Biau, D., Soueid, H. & Bottaro, A. 2008 Transition to turbulence in duct flow. *J. Fluid Mech.* **596**, 133–142.

Boeck, T., Krasnov, D., Thess, A. & Zikanov, O. 2008 Large-scale intermittency of liquid-metal channel flow in a magnetic field. *Phys. Rev. Lett.* **101** (24), 244501-1–244501-4.

Branover, H. 1978 *Magnetohydrodynamic Flow in Ducts*. John Wiley.

Cukierski, K. & Thomas, B. G. 2008 Flow control with local electromagnetic braking in continuous casting of steel slabs. *Metall. Mater. Trans.* B **39** (1), 94–107.

Galletti, B. & Bottaro, A. 2004 Large-scale secondary structures in duct flow. *J. Fluid Mech.* **512**, 85–94.

Gerard-Varet, D. 2002 Amplifcation of small perturbations in a Hartmann layer. *Phys. Fluids* **14**, 1458–1467.

Hartmann, J. & Lazarus, F. 1937 Hg-dynamics. Part II. Experimental investigations on the flow of mercury in a homogeneous magnetic field. *Mat.-Fys. Medd. K. Dan. Vidensk. Selsk.* **15** (7), 1–45.

Hof, B., van Doorne, C., Westerweel, J. & Nieuwstadt, F. 2005 Turbulence regeneration in pipe flow at moderate Reynolds numbers. *Phys. Rev. Lett.* **95**, 214502.

Kobayashi, H. 2008 Large eddy simulation of magnetohydrodynamic turbulent duct flows. *Phys. Fluids* **20**, 015102.

Krasnov, D., Rossi, M., Zikanov, O. & Boeck, T. 2008 Optimal growth and transition to turbulence in channel flow with spanwise magnetic field. *J. Fluid Mech.* **596**, 73–101.

Krasnov, D. S., Zienicke, E., Zikanov, O., Boeck, T. & Thess, A. 2004 Numerical study of instability and transition to turbulence in the Hartmann flow. *J. Fluid Mech.* **504**, 183–211.

Landahl, M. 1980 A note on an algebraic instability of inviscid parallel shear flows. *J. Fluid Mech.* **98**, 243–251.

Lingwood, R. J. & Alboussière, T. 1999 On the stability of the Hartmann layer. *Phys. Fluids* **11**, 2058–2068.

Moresco, P. & Alboussière, T. 2004 Experimental study of the instability of the Hartmann layer. *J. Fluid Mech.* **504**, 167–181.

Müller, U. & Bühler, L. 2001 *Magnetohydrodynamics in Channels and Containers*. Springer.

Potherat, A. 2007 Quasi-two-dimensional perturbations in duct flows under transverse magnetic field. *Phys. Fluids* **19**, 074104.

Reddy, S. C., Schmid, P. J., Bagget, P. & Henningson, D. S. 1998 On the stability of streamwise streaks and and transition thresholds in plane channel flow. *J. Fluid Mech.* **365**, 269–303.

Reed, C. B. & Picologlou, B. F. 1989 Side wall flow instabilities in liquid metal MHD flow under blanket relevant conditions. *Fusion Technol.* **15**, 705–715.

Schmid, P. J. & Henningson, D. S. 2001 *Stability and Transition in Shear Flows*. Springer.

Smolentsev, S. & Dajeh, D. 1996 The effect of a conducting inclusion on the heat transfer in a fully developed MHD flow in a rectangular channel. *Magnetohydrodynamics* **32**, 331–335.

Smolentsev, S., Moreau, R. & Abdou, M. 2008 Characterization of key magnetohydrodynamic phenomena for PbLi flows for the US DCLL blanket. *Fusion Engng Design* **83**, 771–783.

Tatsumi, T. & Yoshimura, T. 1990 Stability of the laminar flow in a rectangular duct. *J. Fluid Mech.* **212**, 437–449.

Ting, A. L., Walker, J. S., Moon, T. J., Reed, C. B. & Picologlou, B. F. 1991 Linear stability analysis for high-velocity boundary layers in liquid-metal magnetohydrodynamic flows. *Intl J. Engng Sci.* **29** (8), 939–948.

Waleffe, F. 1997 On a self-sustaining process in shear flows. *Phys. Fluids* **9**, 883–900.

Zikanov, O. 1996 On the instability of pipe Poiseuille flow. *Phys. Fluids* **8**, 2923–2932.